ISSN 0020-4412, Instruments and Experimental Techniques, 2023, Vol. 66, No. 3, pp. 423–434. © Pleiades Publishing, Ltd., 2023.
Russian Text © The Author(s), 2023, published in Pribory i Tekhnika Eksperimenta, 2023, No. 3, pp. 67–79.

GENERAL EXPERIMENTAL TECHNIQUE

Planar Michelson Interferometer Using Terahertz Surface Plasmons

V. V. Gerasimov[a,c,*], A. K. Nikitin[b], and A. G. Lemzyakov[a]

[a] *Budker Institute of Nuclear Physics SB RAS, Novosibirsk, 630090 Russia*

[b] *Scientific and Technological Center for Unique Instrumentation of the Russian Academy of Sciences, Moscow, 117342 Russia*

[c] *Novosibirsk State University, Novosibirsk, 630090 Russia*

**e-mail: v.v.gerasimov3@gmail.com*

Received September 29, 2022; revised December 17, 2022; accepted December 26, 2022

Abstract—The optical scheme and technical characteristics of terahertz planar Michelson interferometer based on surface plasmons are presented. A technique for determination of the complex index of refraction of surface plasmons ($\tilde{n}_s = n_s + i\kappa_s$) from interferograms is described. The paper presents the results of test measurements on flat surfaces with gold sputtering coated by ZnS layers 0 to 3 μm thick with application of the high-power coherent radiation from the Novosibirsk free electron laser at the wavelength $\lambda_0 = 141$ μm. From the measurement results, the value of the effective permittivity of the sputtered gold surface was found, which turned out to be an order of magnitude lower than that of crystalline gold. Analysis of the energy losses in the plasmonic interferometer made it possible to estimate its dynamic range (10^6–10^8 in terms of radiation power) required for measurements on samples with different $\tilde{n}_s$. Ways to increase the signal-to-noise ratio via optimization of the elements of the optical scheme and detector have also been proposed.

DOI: 10.1134/S0020441223030053

1. INTRODUCTION

Intensive mastering of the terahertz (THz) range of electromagnetic waves with frequency of 0.3 to 10 THz (which corresponds to wavelengths of 1 mm to 30 μm) began only in the 1980s; previously, it was hampered by the lack of high-power sources and sensitive receivers of THz radiation. With the creation of gas and semiconductor THz lasers and then free electron lasers (FELs) and femtosecond lasers, as well as the invention of photoconductive dipole antennas and cryogenic bolometers, the development of THz optics accelerated [1].

An important field of application of THz radiation is spectroscopy because namely the THz range comprises the frequencies of the vibrational and rotational degrees of freedom of a large number of organic, polymeric, and biological molecules, as well as of intermolecular bonds [2]. One of the branches of spectroscopy is the exploration of surface and its transition layer. The thickness of the transition layer for most problems at THz frequencies is much less than the radiation wavelength λ_0, and therefore the probing radiation reflected by the surface carries mainly information about the optical properties of the substrate, not its transition layer. For this reason, well-known methods such as reflection absorption spectroscopy [3] and ellipsometry [4, 5] have insufficient sensitivity in the THz range. This problem is especially relevant when objects under study are localized on a metal or semiconductor substrate because due to the high reflectivity of these materials in the THz range, the intensity of the probe radiation field within the layer under study tends to zero when reflectometry measurements are applied [6].

The use of surface plasmons (SPs), a variant of surface electromagnetic waves generated by a probing radiation on the surface of metals, makes it possible to improve the sensitivity of measurements due to increase in both the length of interaction between the radiation and the layer and the concentration of the radiation field in the near-surface region [7]. Surface plasmons are a complex of the wave of the density of conduction electrons in the near-surface layer of the metal and a *p*-polarized electromagnetic wave, the field of which decays exponentially with increasing distance from the metal-dielectric (environment) interface. In the IR and THz ranges, the simplest and most reliably measured characteristic of SPs is their propagation length L (the distance at which the wave intensity decreases by the factor $e \approx 2.718$). That is why surface plasmon absorption spectroscopy has become more popular [8]. Plasmonic phase spectroscopy is less common, used at measurement of the phase jump during surface probing under conditions of surface plasmon resonance in the visible range [9, 10], or at

determination of the phase shift of SPs in the mid-IR [11] and THz ranges [12] after the SPs have run a macroscopic distance.

Interferometry in beams of SPs or bulk waves produced by SPs enables combining the possibilities of amplitude and phase measurements for determination of the complex refractive index of SPs $\tilde{n}_s = n_s + i\kappa_s$, which is unambiguously related to the dielectric permittivity of the metal and optical constants of the transition layer (by the SP dispersion equation for this waveguide structure) [7, 8]. In addition, plasmonic interferometry enables study of fast processes on a conducting surface and can be efficiently used for sensor applications and in plasmonic microscopy [9, 10].

Plasmonic interferometry has found wide application in visible-range optical sensor devices due to the following features of SPs at these frequencies: short propagation length (which meets the requirement of miniaturization of sensors) and high concentration of the plasmon field (which ensures high sensitivity of devices to changes in the optical characteristics of the sensor layer on the metal surface) [13]. In such devices, as a rule, interference of broadband SPs, generated by white light on two parallel slits (grooves) in an opaque conductive layer, is observed [14]. SPs that propagate normally to the slits interfere with each other, and the result of their interaction is analyzed with application of spectrometer, located either at one of the slits or at the surface between the slits [15, 16].

Test experiments on plasmonic interferometry were also performed in the mid-IR range with application of CO_2 laser [17–19]. The laser radiation beam was directed through the transparent substrate to the edge of the opaque wedge-shaped metal layer deposited on the substrate and covered (for greater stability of SPs) with the subwavelength dielectric layer. Because of the radiation diffraction at the edge of the metal wedge, SPs were generated with some efficiency at the metal-dielectric interface, as was a bulk wave, propagating in the environment at a grazing angle to the surface. Having reached the opposite edge of the metal layer, the surface plasmons were diffracted by it and converted into another bulk wave, emitted from the edge at some angle to the plane of the substrate. In the area of intersection of both bulk waves, an interference pattern was formed, which contained information about the refractive index of the SPs and their attenuation coefficient.

The possibility of creating a plasmon-polariton Mach–Zehnder interferometer for sensing applications in the THz range was considered in [20]. The main difference between the scheme proposed here and those known for the visible range is the use of indium antimonide (InSb) as the material of the layer that guides surface plasmon polaritons (SPPs), for miniaturization of the sensor. The InSb plasma frequency ω_p is in the THz range rather than in the near ultraviolet range (as for noble metals) [21], which ensures closeness of the frequency ω of the radiation generating SPPs to ω_p (more precisely, $\omega \lesssim \omega_p/\sqrt{2}$), i.e., fulfillment of the condition of comparability of L with λ.

However, plasmonic THz interferometers containing a metal (not a semiconductor) surface and thus using SPs with large propagation length can be effectively applied for quality control of the surface of metal and metallized mirrors of macroscopic dimensions; determination of the effective permittivity of metal coatings used in THz plasmon waveguides, metasurfaces, and diffraction gratings; spectroscopy of thin dielectric films on a conducting surface; various sensor applications [22].

The first scheme of the THz Mach–Zehnder interferometer based on surface plasmons was proposed in [23]. In this device, the monochromatic radiation of the source, prior to its interaction with the metal surface, is divided into two beams: the reference and measurement ones. The latter is transformed into SPs, which, after running a certain distance on the surface, hit the wedge-shaped mirror moving along the SP track to transform the surface wave into the bulk one. The bulk waves of both beams overlap and interfere, and the intensity of their resulting field is recorded by a photodetector. The sequence of receiver signals recorded as the distance traveled by the SPs changes is an interferogram, containing information about both parts of the complex refractive index of the SPs.

Later on, schemes of static IR and THz interferometers based on SPs were proposed [24, 25], on the basis of which the theory of dispersive Fourier-transform IR spectroscopy was developed [26]. Because it is difficult to separate the useful signal of SPs and parasitic bulk waves generated on the coupling element and the components of the optical circuit, no experiments using these circuits were carried out.

In some schemes, parasitic bulk waves are used as a reference beam for interference with plasmons. For example, work [27] realized dynamic plasmonic refractometry of a conducting surface, in which the bulk waves generated on the waveguide coupling element interfered with the surface waves. Owing to the single-mode (TM_0) tuning of the plane-parallel waveguide, the spurious bulk waves arising from diffraction at the output of the waveguide had a narrow radiation pattern and propagated in parallel to the conducting surface, just like the SPs generated by the waveguide. As noted by the authors, despite its originality and simplicity, this method can be implemented only for high-impedance surfaces, for which the phase velocity of SPs is noticeably lower than the velocity of a bulk wave in the medium above the surface under study.

With the development and mastering of the technique of reflection and splitting of THz SPs by flat mirrors and beam-splitting plates [28, 29], a scheme of a THz Michelson interferometer based on SPs [30]

was proposed, which was soon tested on FEL radiation [31].

The present work describes the design of a prototype model of the terahertz Michelson interferometer based on SPs and the features of measurements with it; a technique for determination of the complex refractive index of SPs from interferograms is presented, as are the results of identification of the effective permittivity of the deposited gold within its skin layer from the measured characteristics of the SPs at a wavelength of 141 μm.

2. DESIGN OF THZ MICHELSON INTERFEROMETER BASED ON SURFACE PLASMONS

Functioning of a THz SP interferometer, like that of the classical Michelson interferometer, relies on analysis of interferogram. However, this interferogram is formed not by bulk waves, but by collinear SP beams directed by the surface under study [30]. The real part n_s of the SP refractive index is determined via comparison of the FEL emission spectrum with the SP spectrum, resulting from the Fourier analysis of the interferograms. The imaginary part κ_s is governed by the attenuation of the intensity of SPs as they propagate along the surface under study.

The main problems we encountered when creating the planar plasmonic interferometer in the THz range was the need to increase the signal-to-noise ratio, raise the rate of interferogram recording, and reduce the spurious illumination of the receiver. Ways to solve these problems are obvious: 1) use of a high-power source of monochromatic THz radiation; 2) enhancement of the efficiency of the conversion of the source radiation into SPs; 3) decrease in the energy losses of SPs in the optical circuit of the interferometer; 4) application of sensitive and quite fast receivers of THz radiation; 5) spatial separation of spurious bulk waves from SPs and screening of the receiver from spurious illumination. The methods for solving these problems will be presented, to one degree or another, in the description of the design of the plasmonic interferometer in this section.

The source of THz radiation was the Novosibirsk Free Electron Laser (NovoFEL) [32], whose power (along with that of gyrotrons) is currently one of the highest. The NovoFEL radiation is a periodic sequence of 100-ps pulses following at a frequency of 5.6 MHz; it is linearly polarized and completely coherent in the beam cross section; the temporal coherence is 30–100 ps (depending on the operating mode of the laser). The characteristic average power of the radiation arriving at the interferometer input is 30–40 W (if necessary, it can be increased to 400 W); the Gaussian beam diameter is 12 mm. The operating radiation wavelength λ_0 was chosen to be 141 μm with a line width of less than 1%.

Because the spectrum of NovoFEL radiation is unstable in the normal mode of operation (the wavelength can shift by up to 0.2 μm during measurements), for the spectrum variations to be taken into account, the plasmonic interferogram was recorded simultaneously with the interferogram formed by the NovoFEL radiation beams. To this end, the Michelson interferometer for bulk waves was added to the scheme of the plasmonic interferometer [31] (Fig. 1a).

The lithographic polarizer P_1 extracted the *p* component, corresponding to the polarization of SPs from the NovoFEL beam coming to the input of the setup. The 30-μm polypropylene film splitter BS_1 separated the linearly polarized radiation into two beams. The mirror M_5 directed the reflected beam, the intensity of which was controlled by the polarizer P_2, to the bulk-wave interferometer. The cylindrical metal reflecting lens CL with focal length of 75 mm focused the transmitted beam onto the upper edge of the end face of the flat substrate of the sample, where, due to diffraction, the radiation was converted into SPs. In comparison with other known methods (generation on a diffraction grating, waveguide, or flat screen edge), the method of SP generation on the edge of a flat substrate ("the end-fire coupling technique" [33]) features high efficiency (tens of percent at sufficient overlapping of the incident wave fields and SPs [34]), simplicity, and small dispersion of the conversion coefficient.

In the plasmonic interferometer, the fixed and movable mirrors M_1 and M_2 were used (40 × 20 × 5 mm glass plates with gold coating on the reflecting faces and ZnS protective layer). The splitter was the 40 × 25 × 1 mm plane-parallel plate BS_2, made of polyimide material Zeonex (TYDEX, Russia) [35] and installed at an angle of 45° to the incident SP beam. The lower faces of the mirrors and splitter were optically polished and adhered tightly to the substrate, providing optical contact with its surface. Unlike other well-known elements used to reflect or split SPs (Bragg gratings [36] or geodesic prisms [37] formed on the sample surface), flat mirrors and splitters create much fewer parasitic bulk waves in interaction with SPs [29]. In addition, such elements can be rearranged easily during reconfiguration of the interferometer.

As substrates for the test samples, 100 × 150 × 11 mm flat glass plates were used, the upper face of which (100 × 150 mm) was optically polished. An opaque layer of gold 300 nm thick was applied to it by magnetron sputtering, over which a layer of zinc sulfide (ZnS) of uniform thickness was deposited by electron-beam evaporation. Three samples were fabricated: uncoated one and those with the ZnS layer of thickness *d* equal to 1.0 and 3.0 μm. Such a choice of samples was due to the significant difference (according to calculations) in the indices of refraction n_s and absorption κ_s of SPs on these samples, which made it possible to estimate the dynamic range of the interferometer.

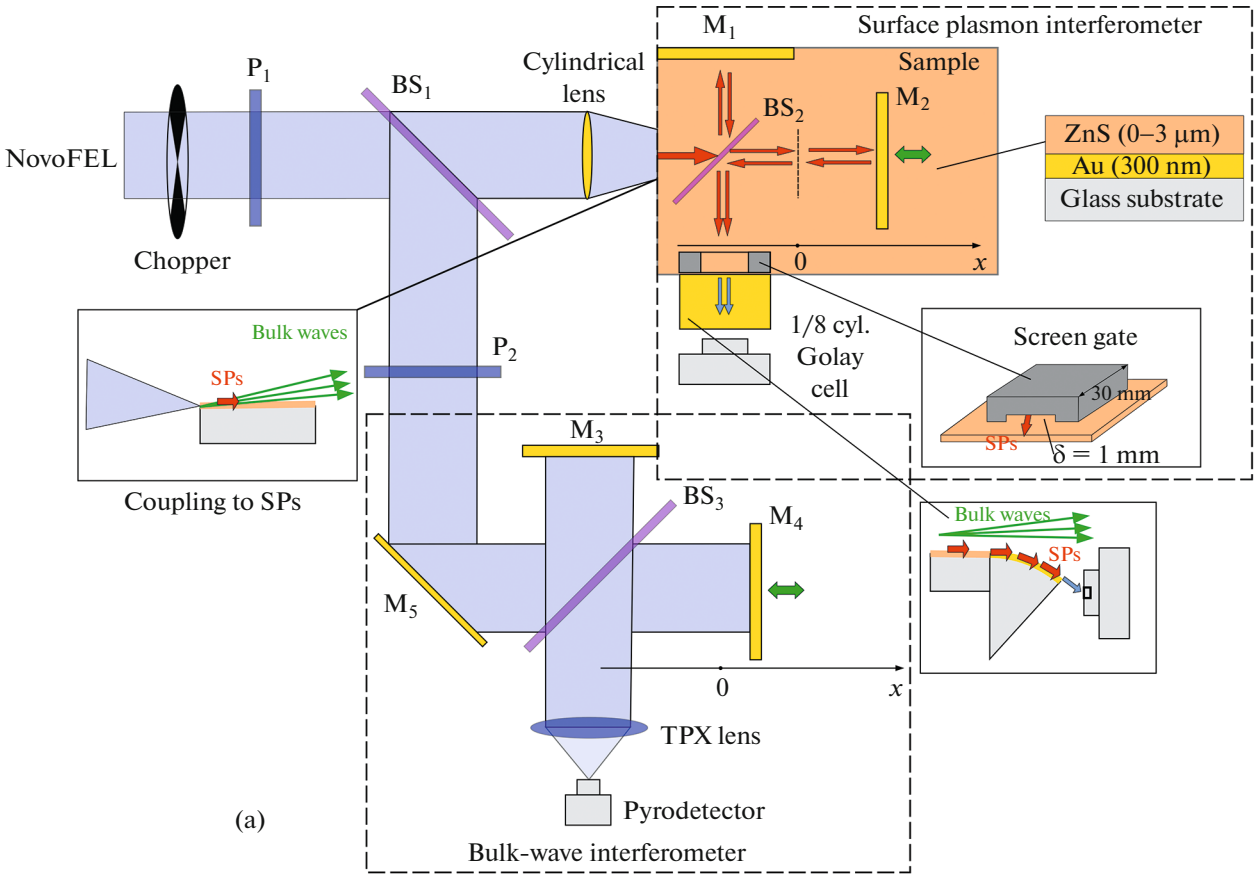

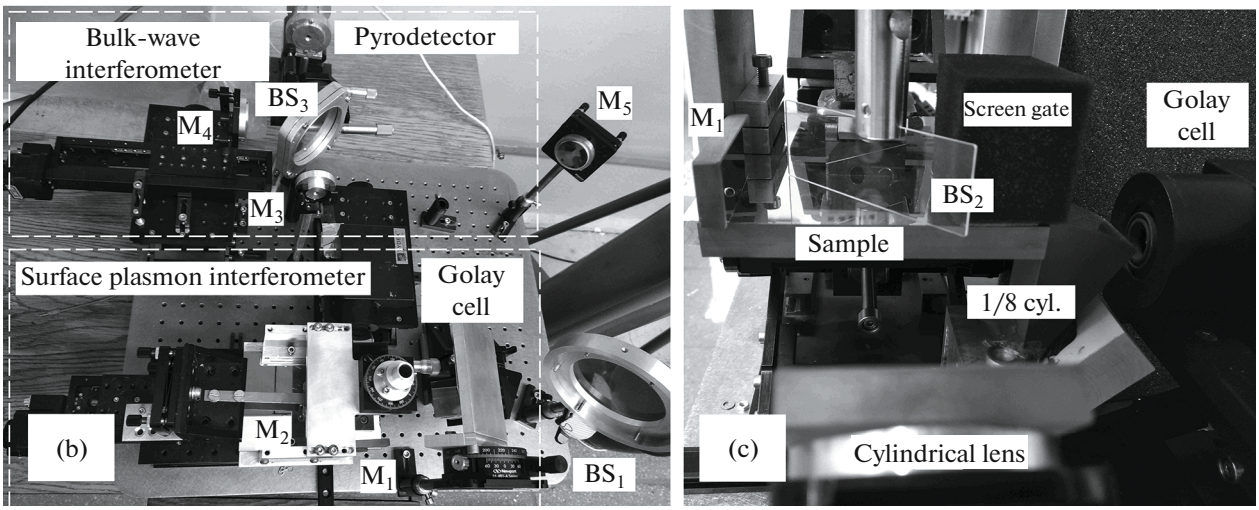

Fig. 1. (a) Optical circuit (top view) of plasmonic THz interferometer: P_1 and P_2 – polarizers; BS_1–BS_3 – beam splitter; M_1–M_5 – flat mirrors; CL – cylindrical reflective lens; TPX lens – lens made of TPX; (b, c) top and side views of plasmonic interferometer.

From the place of generation to the exit from the sample, the SPs passed a distance of about 160 mm. At the output of the plasmonic interferometer, the combined SP beams from both arms went to the convex surface of the cylindrical element (adjacent to the side face of the substrate) for conversion of the SPs into bulk waves. The element was 1/8 of a cylinder with curvature radius of 60 mm, the convex surface of which contained a gold layer 300 nm thick coated by a ZnS layer 1.0 μm thick. The losses (mainly radiative) of the SPs on the cylindrical surface were as high as 99%, although they were minimal at the chosen coat-

ing thickness [38]. Having reached the opposite edge of the convex face of the element, the SPs diffracted on it and converted into bulk waves, which were recorded by the radiation detector. The choice of the cylindrical coupling element was caused by the necessity of spatial separation of the bulk waves generated by the SPs on the output edge of this element from the parasitic bulk waves that arose during 1) the conversion of the NovoFEL radiation into SPs (accompanied by the formation of diffracted bulk waves of high intensity) [39], 2) SP diffraction on the splitter and interferometer mirrors [29], and 3) transition of SPs from the substrate to the output coupling element. Besides that, an additional source of parasitic bulk waves was the scattering [40] of the SPs on the roughness and optical inhomogeneities of the surface of the gold layer, which led to the appearance of radiative losses of SPs [41]. An additional and effective screen against spurious bulk waves was the foam "gate" (35 mm long with the aperture 1 mm high) placed on the sample at the point of its contact with the output coupling element.

The interfering bulk waves generated by the SP beams on the free edge of the output coupling element were detected by the optoacoustic receiver (Golay cell GC-1T, TYDEX, Russia) with high sensitivity ($NEP \approx 1.4 \times 10^{-10}$ W/Hz$^{1/2}$ [42, 43]) and sufficient operation speed (receiver response time of 30 ms). The need to use a highly sensitive receiver was due to the low signal intensity because of the large losses of SPs during their diffraction on the circuit elements and attenuation of the SPs while running along the sample.

In the interferometer for bulk waves, the beams lost energy insignificantly (only upon reflection from the splitter BS_3). Therefore, interferograms of bulk waves were recorded by a less sensitive ($NEP \approx 1.9 \times 10^{-9}$ W/Hz$^{1/2}$) single-pixel pyroelectric receiver MG-33 (NZPP Vostok, Russia) [44, 45], having however high speed (the typical time of receiver heating is about 10 μs [46] and the response time is about 5 ms). The radiation directed to its sensitive element of 1 × 1 mm in size was collected by the TPX lens (TYDEX, Russia) with focal length of 50 mm.

Since the receivers used can record only a radiation flux that varies in time, a mechanical obturator was placed at the input of the setup to modulate the radiation intensity at a frequency of 100 Hz. The signals from each receiver were recorded by two SR-830 synchronous detectors (Stanford Research, USA) with integration time constant of 10 ms (corresponding to the modulation frequency). From the outputs of the detectors, the signals arrived at a two-channel digital oscilloscope (Handyscope 3, TiePie engineering, the Netherlands), which operated in the recorder mode. The measured time dependences were digitized and written to a file.

The movable mirrors M_2 and M_4 were attached to the platforms of motorized shifters (8MT175-50, Standa, Lithuania), which ensured motion of the mirrors during scanning along the x axis with a step of 2.5 μm. The scanning speed was chosen as the maximum possible (250 μm/s) at which the detectors had time to record signals correctly. The recording time for one pair of interferograms corresponding to a displacement of the movable mirrors by 30 mm was about 2 min.

3. MEASUREMENT TECHNIQUE

Before measurements in the THz frequency range, the optical circuits of both interferometers were aligned with respect to the collimated diode laser beam ($\lambda_0 = 635$ nm). The alignment should be carried out with the high accuracy required for determination of the SP refractive index n_s, which exceeds unity by just about 10^{-4} on the uncoated metal. In addition, after change of the sample, it is necessary to align the plasmonic interferometer once more, which takes a long time if the high accuracy is maintained. To reduce the time spent on the alignment and to take into account the slight misalignment between the interferometers, we carried out the measurements in two stages. First, two interferograms were recorded simultaneously (with the use of the plasmonic interferometer and the bulk-wave interferometer) according to the scheme described in Section 2 for SPs propagating along a sample. At the second stage of the measurements, two interferograms were also recorded simultaneously (with the use of the plasmonic interferometer and the bulk-wave interferometer), but that time the NovoFEL radiation was not converted in the plasmonic interferometer into SPs; it was directed to the splitter BS_2 for recording of the interferogram formed by the source radiation in the environment (air). The control interferogram recorded with the bulk-wave interferometer contained information on possible changes in the NovoFEL generation spectrum. Thus, with the two stages of measurements for each sample (which differed in the thickness of the ZnS layer), two pairs of interferograms were obtained. At the same time, for collection of statistics, measurements were repeated four times for each of the samples.

The procedure for alignment of the plasmonic interferometer with launching of SPs is worth a separate description. A fan of parasitic bulk waves of high intensity occurred in the optical circuit of the interferometer (at the conversion of the source radiation into SPs and on the elements of the optical circuit). Some of them could get into the detector, and it was not always possible to determine the presence of a spurious signal in them in the recorded interferograms. At the high measurement accuracy required, this will lead to large errors. For verification if the signal recorded by the receiver was really caused by SPs, not by parasitic waves, an absorber in the form of 10 × 40 mm strips of office paper 0.1 mm thick was placed on different parts of the SP track in one of the arms of the interferome-

Table 1. Attenuation of SP signal (I_0/I) in arms of interferometer after application of paper absorber

Sample	Depth of penetration of SP fields into air, mm (experimental data [41])	Attenuation in arm	
		with movable mirror M_2	with fixed mirror M_1
Au ($d = 0$)	0.75	2.5 ± 0.4	2.9 ± 0.4
Au + ZnS ($d = 1.0$ μm)	0.12	50 ± 8	50 ± 8
Au + ZnS ($d = 3.0$ μm)	0.08	Suppression of signal-to-noise level	

ter. The other arm was completely covered by a foam screen (the signal from this arm did not reach the receiver). If the placement of the paper strip led to the same signal decrease regardless of the arm and position of the absorber on the SP track, this fact confirmed the plasmonic nature of the recorded signal [39]. If the attenuation of the signal depended on the location of the absorber, this indicated that the "diffraction satellites" generated by the diffraction of SPs on the absorber hit the receiver.

As an illustration, Table 1 presents the attenuation of SP signals as the ratio of the initial signal I_0 in an arm to the signal I after the placement of the absorber. It can be seen that the attenuation in both arms is the same within the measurement error. With increase in the coating thickness d, the absorption of SPs grows due to the increase in the concentration of the SP field in the near-surface region of the sample (see the second column *Depth of SP penetration into air*). For the sample with $d = 3.0$ μm, the useful signal was completely suppressed to the noise level, since almost the entire field of the surface wave interacted with the absorber.

Figure 2a presents an example of plasmonic interferograms and interferograms of bulk waves recorded on the sample with $d = 1.0$ μm. As the movable mirrors of the interferometers are displaced along the x axis, the amplitudes of the sinusoids first increase, then reach the maximum, and decrease in the final section of the scanning. This is a typical symmetrical form of autocorrelation function for a coherent radiation source [47]. The amplitude envelope has a Gaussian profile, the width of which determines the length (time) of coherence, which was 30 mm (100 ps) in this experiment. This value coincides with the maximum duration of the NovoFEL radiation pulse during operation in a stable mode.

Then the spectra of the SPs and NovoFEL radiation were calculated from the interferograms with application of the Fourier transform (Fig. 2b). The empty dots in this figure indicate the results of calculations of the components of the Fourier spectrum. Note that the number of calculated points is governed by the interferogram length, which depends on the length of coherence of the NovoFEL radiation ($l_{coh} \approx 30$ mm). Next, the spectra were approximated with the Gaussian

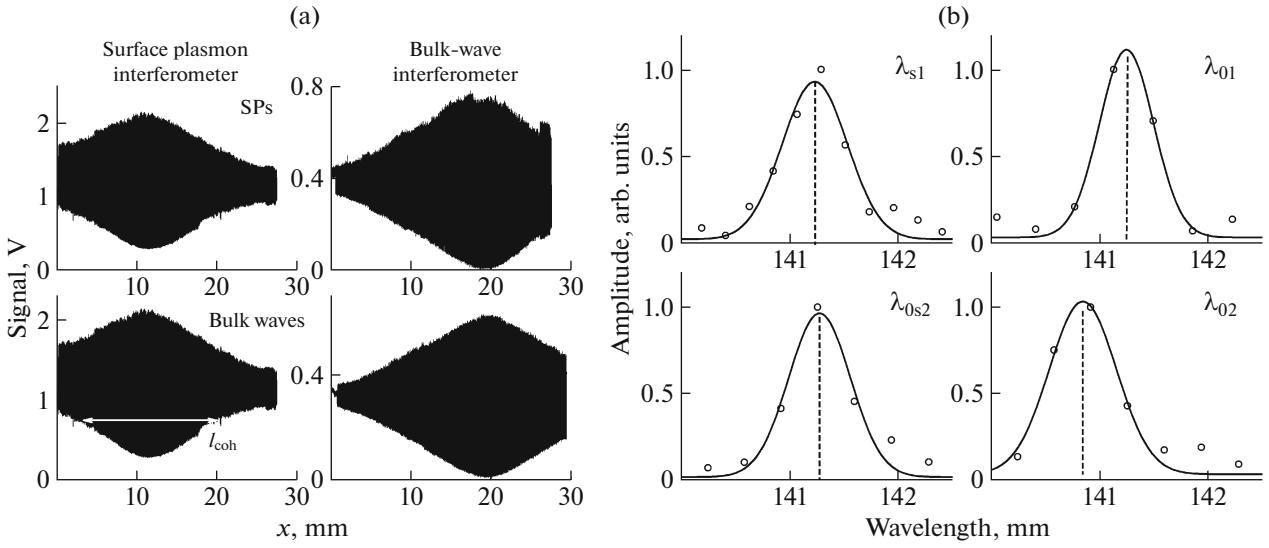

Fig. 2. (a) Example of interferograms obtained with plasmonic interferometer (left) and bulk-wave interferometer (right) for sample "Au + ZnS layer 1.0 μm thick"; top row: graphs with SP excitation; bottom row: graphs without SP excitation; (b) Fourier spectra of SPs and NovoFEL radiation generating them, reconstructed from interferograms in Fig. 2a (empty dots) and approximation of spectra by Gaussian function (solid curve).

function of the form $f(x) = A\exp\left[-\frac{1}{2}\left(\frac{x-x_c}{w}\right)^2\right] + f_0$ and normalized to the value $(A + f_0)$. The w value defines the spectrum width. The value of the parameter x_c, which determines the position of the central line of the spectrum, corresponds to the desired wavelength. The x_c value coincides completely with the results of the direct (but much more laborious) method of calculation of the wavelength from the average period of interferogram. The following wavelengths (central lines of the spectra) are marked in Fig. 2b: λ_{s1} and λ_{0s2}, found from the interferograms in Fig. 2a, obtained on the plasmonic interferometer with and without SP excitation, respectively; λ_{01} and λ_{02} – corresponding to these interferograms wavelengths of NovoFEL radiation in air, determined with the use of the bulk-wave interferometer.

Since the complex refractive index $\tilde{n}_s$ of SPs is defined as the ratio of the wave number k_s of SPs to the wave number of the source radiation in vacuum $k_0 = 2\pi/\lambda_0$,

$$\tilde{n}_s = \frac{k_s}{k_0} = n_s + i\varkappa_s, \quad (1)$$

the real part n_s can be found from the spectra presented in Figs. 2b according to the following formula:

$$n_s = \left(\frac{\lambda_{s1}/\lambda_{0s2}}{\lambda_{01}/\lambda_{02}}\right)\mathrm{Re}(\tilde{n}_a), \quad (2)$$

where the ratio $\lambda_{s1}/\lambda_{0п}$ is defined by expression (1), and the normalization to $\lambda_{01}/\lambda_{02}$ takes into account the shift in the NovoFEL radiation spectrum that can occur during the time between recordings of interferograms with and without SP excitation (see Section 2). The factor $\mathrm{Re}(\tilde{n}_a)$ in expression (2) makes it possible to take into account the fact that laser radiation propagates not in vacuum, but in air with the complex refractive index $\tilde{n}_a = 1.0002726 + i0.0000039$ [48, 49]. For each sample, the average value of n_s was found for four sets of interferograms.

To find the κ_s value, we measured the decrease in the SP intensity at displacement of the movable mirror M_2 (see Fig. 1) in the plasmonic interferometer; in this case, the fixed mirror M_1 was covered by the absorbing plate. The characteristic form of the dependence measured on the sample with the ZnS layer 1 μm thick is shown in Fig. 3. The same figure shows the result of approximation of the measurement results by a function of the form $g(x) = B\exp(-2x/L) + g_0$. The exponent indicator takes into account the fact that the SP path increased by $2x$ when the mirror M_2 was displaced by x. The noise level g_0 was measured experimentally and served as an approximation parameter (for the plot shown in Fig. 3, the noise level was almost zero). For each sample, the average length L_{av} of SP

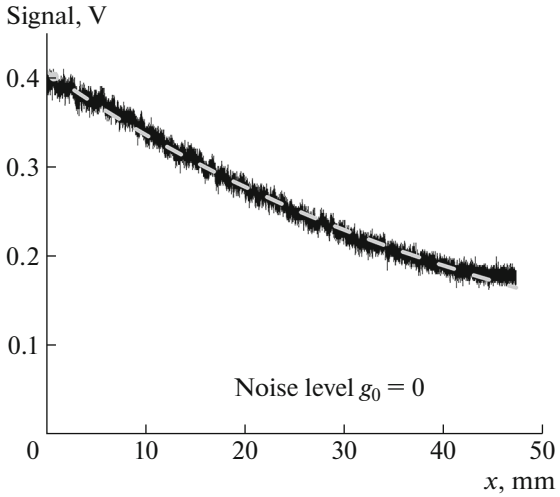

Fig. 3. Attenuation of SP intensity on sample "Au + ZnS layer 1.0 μm thick" at displacement x of mirror M_2 (see Fig. 1a) in plasmonic interferometer and fixed mirror M_1 closed by absorber. Gray dashed line: result of exponential approximation.

propagation was found from the results of several successive measurements (four measurements in our case), and the κ_s value was calculated by the formula [7]

$$\kappa_s = \frac{\lambda_0}{4\pi L_{av}}. \quad (3)$$

4. RESULTS OF TEST MEASUREMENTS

Table 2 presents the values of the real (without unity) and imaginary parts of the refractive index of SPs, found by formulas (2) and (3) for the three samples. For comparison, the same table shows the values of these quantities calculated from the SP dispersion equation for the three-layer structure ("gold–ZnS layer–air") at $\lambda_0 = 141$ μm. This dispersion equation has the following form [50]:

$$\tanh(k_0 d\sqrt{\tilde{n}_s^2 - \varepsilon_d}) = -\frac{\sqrt{\tilde{n}_s^2 - \varepsilon_d}\left(\frac{\sqrt{\tilde{n}_s^2 - \varepsilon_a}}{\varepsilon_a} + \frac{\sqrt{\tilde{n}_s^2 - \varepsilon_m}}{\varepsilon_m}\right)}{\varepsilon_d\left(\frac{\sqrt{\tilde{n}_s^2 - \varepsilon_a}\sqrt{\tilde{n}_s^2 - \varepsilon_m}}{\varepsilon_a\varepsilon_m} + \frac{\tilde{n}_s^2 - \varepsilon_d}{\varepsilon_d^2}\right)}, \quad (4)$$

where d is the thickness of the dielectric coating; ε_m and $\varepsilon_a = \tilde{n}_a^2$ is the permittivity of the metal and the environment, respectively. In these calculations, the refractive index of ZnS was taken as $n_d = 2.943 + i0.01$ [21], and the gold permittivity ε_m was calculated by the Drude model for reference values of the plasma frequency ($\omega_p = 1.37 \times 10^{16}\ \mathrm{s}^{-1}$) and the frequency of col-

Table 2. Refractive indices of SPs (real part without unity ($n_s - 1$) and imaginary part κ_s), calculated at substitution of experimental results into formulas (2) and (3), as well as their calculated values

Sample	$n_s - 1$, 10^{-4}		κ_s, 10^{-4}	
	Experiment	Calculation by Drude model	Experiment	Calculation by Drude model
Au ($d = 0$)	4.9 ± 4	2.7	1.5 ± 0.1	0.014
Au + ZnS (d =1.0 μm)	14 ± 2	10.5	1.1 ± 0.1	0.4
Au + ZnS (d =3.0 μm)	98 ± 10 (112 ± 16 [27])	81	3.7 ± 0.1 (6.6 ± 0.7 [27])	1.3

lisions of conduction electrons ($\omega_\tau = 4.05 \times 10^{13}$ s^{-1}) [51]:

$$\varepsilon_m(\omega) = 1 - \frac{\omega_p^2}{\omega^2 + \omega_\tau^2} + i\frac{\omega_\tau \omega_p^2}{\omega(\omega^2 + \omega_\tau^2)}, \quad (5)$$

where $\omega = 2\pi c/\lambda_0 = 1.34 \times 10^{13}$ s^{-1} (c is the speed of light in vacuum).

According to Table 2, the experimental value of κ_s, which characterizes the losses of SPs at propagation along the sample, is noticeably larger (especially at $d = 0$) than the respective calculated value. This can be because, in addition to the Joule losses in the metal, SPs experience radiation losses on the roughness and optical inhomogeneities of the surface [41]. According to [41], the placement of a dielectric layer on the surface of conductor is expected to lead to decrease in the radiation losses of SPs due to the bigger difference between the refractive index n_s of SPs and the refractive index of the source radiation in air. Moreover, at a sufficiently large thickness of the ZnS layer (d = 1.0 and 3.0 μm), the radiation losses become much lower than the Joule losses, which is expected to lead to coincidence of the calculated and experimental values of κ_s. However, according to Table 2, at d = 1.0 and 3.0 μm, the measured SP losses are approximately three times higher than the calculated ones. It can also be seen that in the experiment the value of ($n_s - 1$) is consistently greater than the calculated values for the respective ZnS layer thicknesses. In our opinion, such discrepancies between the experiment and theory indicate that the effective permittivity of the metal surface differs from its values in crystalline metal calculated by the Drude model, which is most likely due to the granular structure of the surface of the deposited metal layer and its roughness.

For the sample with $d = 3.0$ μm, the result for ($n_s - 1$) coincides within the error with the data of [27], which indicates the reliability of the measurements, whereas the calculated value of κ_s is two times less than the measured one, because the radiative losses of SPs were not taken into account in [27].

From the experimental values of ($n_s - 1$) and κ_s for a sample with a given thickness of the ZnS layer, one can determine the effective permittivity of the metal surface by solving dispersion equation (4) numerically. Table 3 presents solutions for the real and imaginary parts of the permittivity ε_m of the gold plating, found from the data in Table 2. The errors for ε_m correspond to the scatter of solutions to equation (4) with the accuracy of determination of ($n_s - 1$) and κ_s taken into account. Table 3 also shows the gold permittivity values calculated by the Drude model (see formula (5)) with application of reference data for crystalline gold at λ_0 = 141 μm. As can be seen from the table, the experimental values of ε_m are less than the calculated ones by more than an order of magnitude. The largest difference (more than two orders of magnitude) is observed for uncoated gold ($d = 0$), which is due to the fact that the analytical model (Eq. (4)) does not take into account the radiation losses of SPs, which are very substantial for SPs on a conducting surface without a coating dielectric layer. More or less close values of ε_m are observed in the presence on the metal of the ZnS layer with thickness of 1.0 and 3.0 μm, when the radiation losses of SPs are small. We made detail analysis of experimental results obtained with various ZnS dielectric thicknesses, which showed that for correct measurement of the optical constants of metal surface, it is necessary to use dielectric coatings of sufficient thickness.

5. ANALYSIS OF ERRORS AND METHODS TO INCREASE ACCURACY OF DETERMINATION OF PERMITTIVITY OF METAL SURFACE

It is worth paying attention to the very large errors in the experimental values of ε_m in Table 3 (54 to 100%). This is because of the insufficient accuracy of the measurement of ($n_s - 1$) and κ_s (see Table 2), which did not exceed 10% on average. Analysis of Eq. (4) shows that the greatest accuracy requirements relate to n_s. To achieve an accuracy of ε_m determination of 20%, it

Table 3. Values of real and imaginary parts of permittivity ε_m of sputtered gold, found from experimental values of $(n_s - 1)$ and κ_s from Table 2, as well as ε_m values calculated by Drude model (see formula (5)) at $\lambda_0 = 141$ μm

Sample	$\mathrm{Re}(\varepsilon_m)$		$\mathrm{Im}(\varepsilon_m)$	
	Experiment	Calculation by Drude model	Experiment	Calculation by Drude model
Au ($d = 0$)	-800 ± 800	-105000	1700 ± 1500	317000
Au + ZnS ($d = 1.0$ μm)	-5600 ± 3600		2600 ± 1400	
Au + ZnS ($d = 3.0$ μm)	-7000 ± 5000		1000 ± 800	

Table 4. Estimates of energy losses in plasmonic interferometer

*S*ample	Efficiency of generation of SPs	κ_s			Total loss	Signal power at $I_0 = 10$ W
		on flat surface of sample	on splitter of SPs	on cylindrical converting element [38]		
Au ($d = 0$)	<0.001	0.14	0.5	0.01	$<10^{-6}$	< 10 μW
Au + ZnS ($d = 1.0$ μm)	0.3	0.2			$<2\cdot10^{-4}$	< 2 mW
Au + ZnS ($d = 3.0$ μm)	<0.001	0.005			$<2\cdot10^{-8}$	< 200 nW

is necessary to find out n_s with accuracy not worse than 10^{-4} (at an actual error of 10% for κ_s, which depends on the signal-to-noise ratio, alignment, and stability of the NovoFEL radiation intensity). Such accuracy for n_s can be attained if the stability of the radiation source with respect to the wavelength during recording of interferogram is not worse than 0.01 μm (at $\lambda_0 = 141$ μm) and the width of the generation line is an order of magnitude smaller than $1.0 - 1.5$ μm in normal mode operation. This can be achieved via reduction of the measurement time and application of faster and more sensitive detectors. For example, a pyroelectric detector could be used instead of the Golay cell (see Fig. 1), which will enable reduction of the interferogram measurement time by an order of magnitude (up to 10 s per scan). To increase the sensitivity of the pyrodetector, instead of the germanium input window (on which more than half of the incident power is lost because of the Fresnel losses), a transparent dielectric lens could be used. It would reduce the reflection losses and collect the entire beam of bulk waves generated by the SPs darting off the output coupling element to the sensitive element of the receiver. It would also be of interest for applications to use more stable and compact sources of coherent THz radiation than FELs, such as gas lasers [52], backward wave tubes [53], gyrotrons [54], or quantum cascade lasers [55].

The NovoFEL immunity to temporal variations in the radiation wavelength can be better in operation in the mode with negative detuning of the repetition frequency of free electron bunches from the frequency of revolution of light pulses inside the optical cavity of the FEL. Such operation is accompanied by decrease in the average radiation power [56]. When the FEL operates in this regime, a stable single-mode generation regime is established, the linewidth of which is as narrow as possible (0.25%) [47], while the wavelength shift in 15 min is not more than 0.1 of the width of the generated radiation spectrum (0.04 μm at $\lambda_0 = 141$ μm), which is close to the desired accuracy. However, achievement of such generation mode requires long and laborious tuning of the NovoFEL parameters.

A very important parameter that affects the measurement accuracy of both n_s and κ_s is the "useful signal/noise" ratio, which is proportional to the useful signal from SPs arriving at the detector. Table 4 presents estimates of SP losses in the interferometer for the samples used in the experiments described above. These losses are the sum of losses during the generation of SPs at the input to the interferometer and propagation along the surface of the sample and the surface of the cylindrical coupling element (see Fig. 1a). The losses in the diffraction on the splitter and mirrors and in the SP passage from the sample to the coupling element are not taken into account here. From the magnitude of the total losses of the SPs, one can judge on the dynamic range of the "source–detector" complex, which will enable measurements on the plasmonic interferometer. It must be at least 10^4 for the sample

with the minimum losses ($d = 1.0$ μm) and at least 10^8 for the sample with the maximum SP losses ($d = 3.0$ μm). If a THz radiation with an average power of 10 W is incident on the input of the interferometer, then the detector sensitivity threshold should be not worse than 200 nW, which is slightly higher than the sensitivity threshold of the Golay cell used together with a lock-in amplifier (about 10 nW). Therefore, at work with THz radiation sources inferior in power to NovoFEL, for detection of the useful signal in the interferometer it is necessary to use more sensitive detectors.

The requirements for the dynamic range (and detector sensitivity) can be lowered via reduction of the SP losses in the interferometer. This can be achieved in two ways: 1) reducing the size of the interferometer to the minimum values, determined by the size of the cross section of the plasmon beam (it was 12 mm in our case); 2) using a cylindrical coupling element with minimum SP losses on its surface, which are achieved at a certain radius of its curvature; increase in this radius leads, on the one hand, to decrease in the radiation losses, and on the other hand, to higher Joule losses due to the longer SP track on the convex surface.

6. CONCLUSIONS

The paper presents the optical circuit and technical characteristics of a prototype model of planar THz SP Michelson interferometer. A technique for determination of the complex refractive index of SPs ($\tilde{n}_s = n_s + i\kappa_s$) from interferograms is described in detail. The interferometer was tested on flat surfaces with gold sputtering coated with a ZnS layer 0 to 3.0 μm thick with application of high-power coherent radiation of NovoFEL at the wavelength $\lambda_0 = 141$ μm. From the found values of $\tilde{n}_s$ the effective permittivity ε_m of the deposited gold surface was calculated, which turned out to be an order of magnitude lower than that of crystalline gold. The large error for the found values of ε_m is mainly due to the insufficient temporal stability of the emission spectrum of NovoFEL. For practical applications of the plasmonic interferometer, it is necessary to use more stable and compact sources of THz radiation.

Analysis of the energy losses of SPs in the plasmonic interferometer has made it possible to estimate its dynamic range in terms of the radiation power (10^6–10^8) required for measurements on samples with different $\tilde{n}_s$ and suggest methods to increase the signal-to-noise ratio by optimizing the optical elements of the interferometer and the THz radiation detector used in it.

ACKNOWLEDGMENTS

The work was done at the shared research center SSTRC on the basis of the Novosibirsk FEL at BINP SB RAS.

CONFLICT OF INTEREST

The authors have no conflict of interest.

REFERENCES

1. Bratman, V.L., Litvak, A.G., and Suvorov, E.V., *Usp. Fiz. Nauk,* 2011, vol. 181, no. 8, p. 867. https://doi.org/10.3367/UFNe.0181.201108f.0867
2. Ghann, W. and Uddin, J., *Terahertz Spectroscopy: A Cutting-Edge Technology,* Uddin, J., Ed., London: IntechOpen, 2017.
3. O'Hara, J.F., Withayachumnankul, W., and Al-Naib, I., *J. Infrared, Millimeter, Terahertz Waves,* 2012, vol. 33, no. 3, p. 245. https://doi.org/10.1007/s10762-012-9878-x
4. Hofmann, T., Herzinger, C.M., Boosalis, A., Tiwald, T.E., Woollam, J.A., and Schube, M., *Rev. Sci. Instrum.,* 2010, vol. 81, p. 023101. https://doi.org/10.1063/1.3297902
5. Azarov, I.A., Shvets, V.A., Prokopiev, V.Yu., Dulin, S.A., Rykhlitskii, S.V., Kruchinin, V.N., Choporova, Yu.Yu., Knyazev, B.A., and Kruchinina, M.V., *Instrum. Exp. Tech.,* 2015, vol. 58, no. 3, p. 381. https://doi.org/10.1134/S0020441215030033
6. Naftaly, M. and Dudley, R., *Appl. Opt.,* 2011, vol. 50, no. 9, p. 3201. https://doi.org/10.1364/AO.50.003201
7. *Poverkhnostnye polyaritony. Elektromagnitnye volny na poverkhnostyakh i granitsakh razdela sred* (Surface Polaritons. Electromagnetic Waves on Surfaces and Media Boundaries), Agranovich, V.M. and Mills, D.L., Eds., Moscow: Nauka, 1985.
8. Maier, S.A., *Plasmonics—Fundamentals and Applications,* New York: Springer, 2007.
9. Nikitin, A.K. and Tishchenko, A.A., *Pis'ma Zh. Tekh. Fiz.,* 1991, vol. 17, no. 11, p. 76.
10. Huang, Y.H., Ho, H.P., Wu, S.Y., and Kong, S.K., *Adv. Opt. Technol.,* 2012, vol. 2012, p. 471957. https://doi.org/10.1155/2012/908976
11. Silin, V.I., Voronov, S.A., Yakovlev, V.A., and Zhizhin, G.N., *Int. J. Infrared Millimeter Waves,* 1989, vol. 10, no. 1, p. 101. https://doi.org/10.1007/BF01009121
12. Wang, K. and Mittleman, D.M., *Phys. Rev. Lett.,* 2006, vol. 96, p. 157401. https://doi.org/10.1103/PhysRevLett.96.157401
13. Gao, Y., Xin, Z., Gan, Q., Cheng, X., and Bartoli, F.J., *Opt. Express,* 2013, vol. 21, no. 5, p. 5859. https://doi.org/10.1364/OE.21.005859
14. Melentiev, P.N., Kuzin, A.A., Gritchenko, A.S., Kalmykov, A.S., and Balykin, V.I., *Opt. Commun.,* 2017, vol. 382, p. 509. https://doi.org/10.1016/j.optcom.2016.07.061

15. Gan, Q.Q., Gao, Y., and Bartoli, F.J., *Opt. Express,* 2009, vol. 17, no. 23, p. 20747. https://doi.org/10.1364/OE.17.020747
16. Ming, Y., Wu, Z., Wu, H., Xu, F., and Lu, Y., *IEEE Photonics J.,* 2012, vol. 4, no. 1, p. 491. https://doi.org/10.1109/JPHOT.2012.2186562
17. Schlesinger, Z. and Sievers, A.J., *Appl. Phys. Lett.,* 1980, vol. 36, no. 6, p. 409. https://doi.org/10.1063/1.91519
18. Hanssen, L.M., Riffe, D.M., and Sievers, A.J., *Opt. Lett.,* 1986, vol. 11, no. 12, p. 782. https://doi.org/10.1364/OL.11.000782
19. Petrov, Yu.E., Alieva, E.V., Zhizhin, G.N., and Yakovlev, V.A., *Zh. Tekh. Fiz.,* 1998, vol. 68, no. 3, p. 64.
20. Ma, Y., Nguyen-Huu, N., Zhou, J., Maeda, H., Wu, Q., Eldlio, M., Pistora, J., and Cada, M., *IEEE J. Sel. Top. Quantum Electron.,* 2017, vol. 23, no. 4, p. 4601607. https://doi.org/10.1109/JSTQE.2017.2660882
21. *Handbook of Optical Constants of Solids,* Palik, E.D., Ed., Academic, 2016, vol. 1.
22. Pandey, S., Gupta, B., Chanana, A., and Nahata, A., *Adv. Phys.,* 2016, vol. 1, no. 2, p. 176. https://doi.org/10.1080/23746149.2016.1165079
23. Zhizhin, G.N., Nikitin, A.K., Balashov, A.A., and Ryzhova, T.A., RF Patent 2318192, *Byull. Izobret.,* 2008, no. 6.
24. Bogomolov, G.D., Zhizhin, G.N., Kiryanov, A.P., Nikitin, A.K., and Khitrov, O.V., *Bull. Rus. Acad. Sci.: Phys.,* 2009, vol. 73, no. 4, p. 533. https://doi.org/10.3103/S1062873809040224
25. Nikitin, A.K., Knyazev, B.A., Gerasimov, V.V., and Khasanov, I.Sh., RF Patent 2653590, *Byull. Izobret.,* 2018, no. 14.
26. Zhizhin, G.N., Kiryanov, A.P., and Nikitin, A.K., *Opt. Spectrosc.,* 2012, vol. 112, no. 4, p. 545. https://doi.org/10.1134/S0030400X12040248
27. Gerasimov, V.V., Knyazev, B.A., Nikitin, A.K., Nikitin, V.V., and Rijova, T.A., *Discrete and Continuous Models and Applied Computational Science,* 2013, no. 2, p. 191. https://journals.rudn.ru/miph/article/view/8543.
28. Gerasimov, V.V., Knyazev, B.A., and Nikitin, A.K., *Quantum Electron.,* 2017, vol. 47, no. 1, p. 65. https://doi.org/10.1070/QEL16178
29. Gerasimov, V.V., Nikitin, A.K., Lemzyakov, A.G., Azarov, I.A., Milekhin, I.A., Knyazev, B.A., Bezus, E.A., Kadomina, E.A., and Doskolovich, L.L., *J. Opt. Soc. Am. B,* 2020, vol. 37, no. 5, p. 1461. https://doi.org/10.1364/JOSAB.386331
30. Nikitin, A.K. and Khitrov, O.V., RF Patent 2709600, *Byull. Izobret.,* 2019, no. 35.
31. Gerasimov, V.V., Nikitin, A.K., Khitrov, O.V., and Lemzyakov, A.G., *Proc. 6th Int. Conference on Infrared, Millimeter, and Terahertz Waves (IRMMW-THz),* Chengdu, August 29–September 3, 2021, p. 1. https://doi.org/10.1109/IRMMW-THz50926.2021.9567134.
32. Shevchenko, O.A., Vinokurov, N.A., Arbuzov, V.S., Chernov, K.N., Davidyuk, I.V., Deichuly, O.I., Dementyev, E.N., Dovzhenko, B.A., Getmanov, Ya.V., Gorbachev, Ya.I., Knyazev, B.A., Kolobanov, E.I., Kondakov, A.A., Kozak, V.R., Kozyrev, E.V., et al., *Bull. Rus. Acad. Sci.: Phys.,* 2019, vol. 83, p. 228. https://doi.org/10.3103/S1062873819020278
33. Stegeman, G.I., Wallis, R.F., and Maradudin, A.A., *Opt. Lett.,* 1983, vol. 8, no. 7, p. 386. https://doi.org/10.1364/OL.8.000386
34. Kotelnikov, I.A., Gerasimov, V.V., and Knyazev, B.A., *Phys. Rev. A,* 2013, vol. 87, p. 023828. https://doi.org/10.1103/PhysRevA.87.023828
35. Islam, M.S., Nine, J., Sultana, J., Cruz, A.L.S., Dinovitser, A., Ng, B.W., Ebendorff-Heidepriem, H., Losic, D., and Abbott, D., *IEEE Access,* 2020, vol. 8, p. 97204. https://doi.org/10.1109/ACCESS.2020.2996278
36. Nazarov, M., Garet, F., Armand, D., Shkurinov, A., and Coutaz, J.-L., *C. R. Phys.,* 2008, vol. 9, p. 232. https://doi.org/10.1016/j.crhy.2008.01.004
37. Knyazev, B.A. and Nikitin, A.K., RF Patent 2547164, *Byull. Izobret.,* 2015, no. 10.
38. Knyazev, B.A., Gerasimov, V.V., Nikitin, A.K., Azarov, I.A., and Choporova, Yu.Yu., *J. Opt. Soc. Am. B,* 2019, vol. 36, p. 1684. https://doi.org/10.1364/JOSAB.36.001684
39. Gerasimov, V.V., Knyazev, B.A., Nikitin, A.K., and Nikitin, V.V., *Tech. Phys. Lett.,* 2010, vol. 36, no. 11, p. 1016. https://doi.org/10.1134/S1063785010110131
40. Zayats, A.V., Smolyaninov, I.I., and Maradudin, A.A., *Phys. Rep.,* 2005, vol. 408, p. 131. https://doi.org/10.1016/j.physrep.2004.11.001
41. Gerasimov, V.V., Knyazev, B.A., Lemzyakov, A.G., Nikitin, A.K., and Zhizhin, G.N., *J. Opt. Soc. Am. B,* 2016, vol. 33, p. 2196. https://doi.org/10.1364/JOSAB.33.002196
42. Minin, I.V. and Minin, O.V., *Vestn. SGUGIT (Sib. Gos. Univ. Geosist. Tekhnol.),* 2022, vol. 26, no. 4, p. 160. https://doi.org/10.33764/2411-1759-2021-26-4-160-175
43. http://www.tydexoptics.com/ru/products/thz_devices/golay_cell/.
44. http://www.nzpp.ru/product/gotovye-izdeli/fotopriemnye-ustroystva/.
45. Paulish, A.G., Dorozhkin, K.V., Gusachenko, A.V., Morozov, A.O., and Pyrgaeva, S.M., *Sbornik trudov konferentsii "Aktual'nye problemy radiofiziki APR 2019"* (Proc. Conference "Topical Problems on Radio-Physics APR 2019"), Tomsk, 2019, p. 482. http://vital.lib.tsu.ru/vital/access/manager/Repository/vtls:000709334.
46. Zubov, V.A., *Metody izmereniya kharakteristik lazernogo izlucheniya* (Methods for Measuring Characteristics of Laser Emission), Moscow: Nauka, 1973.
47. Kubarev, V.V., Kulipanov, G.N., Kolobanov, E.I., Matveenko, A.N., Medvedev, L.E., Ovchar, V.K., Salikova, T.V., Scheglov, M.A., Serednyakov, S.S., and Vinokurov, N.A., *Nucl. Instrum. Methods Phys. Res., Sect. A,* 2009, vol. 603, p. 25. https://doi.org/10.1016/j.nima.2008.12.122
48. *Handbook: Physical Data,* Grigoryev, I.S. and Meilikhov, E.Z., Eds., Moscow: Energoatomizdat, 1991.

49. Mathar, R.J., *J. Opt. A: Pure Appl. Opt.,* 2007, vol. 9, p. 470. https://doi.org/10.1088/1464-4258/9/5/008
50. Burke, J.J., Stegeman, G.I., and Tamir, T., *Phys. Rev. B,* 1986, vol. 33, no. 8, p. 5186. https://doi.org/10.1103/PhysRevB.33.5186
51. Ordal, M.A., Long, L.L., Bell, R.J., Bell, S.E., Bell, R.R., Alexander, R.W., and Ward, C.A., *Appl. Opt.,* 1983, vol. 22, p. 1099. https://doi.org/10.1364/AO.22.001099
52. Jiu Zhi-Xian, Zuo Du-Luo, Miao Liang, Qi Chun-Chao, and Cheng Zu-Hai, *Chin. Phys. Lett.,* 2010, vol. 27, p. 024211. https://doi.org/10.1088/0256-307X/27/2/024211
53. Kozlov, G. and Volkov, A., in *Topics in Applied Physics,* vol. 74: *Millimeter and Submillimeter Wave Spectroscopy of Solids,* Grüner, G., Ed., Berlin, Heidelberg: Springer, 2007. https://doi.org/10.1007/BFb0103420
54. Idehara, T., Sabchevski, S.P., Glyavin, M., and Mitsudo, S., *Appl. Sci.,* 2020, vol. 10, p. 980. https://doi.org/10.3390/app10030980
55. Wen, B. and Ban, D., *Prog. Quantum Electron.,* 2021, vol. 80, p. 100363. https://doi.org/10.1016/j.pquantelec.2021.100363
56. Kubarev, V.V., *Doctoral Sci. (Phys.-Math.) Dissertation,* Novosibirsk: Budker Institute of Nuclear Physics Siberian Branch Russ. Acad. Sci., 2016.